VOLATILES IN HIGH TITANIUM BASALTS FROM THE MOON. J. J. Barnes[1,2*], F. M. McCubbin[1], J. W. Boyce[1], A. N. Nguyen[1,3], and S. Messenger[1]. [1]ARES, NASA JSC, Houston, TX. [2]School of Physical Sciences, The Open University, Milton Keynes, U.K. [3]JETS JACOBS, NASA JSC, Houston, TX. *jessica.j.barnes@nasa.gov

Introduction: Chlorine is an unusual isotopic system, being essentially unfractionated (δ^{37}Cl ~ 0 ‰) between bulk terrestrial samples and chondritic meteorites [e.g., 1-2] and yet showing large variations in lunar, martian, and vestan (HED) samples (from ~ -4 to +81‰, [3-10]). Among lunar samples, the volatile-bearing mineral apatite ($Ca_5(PO_4)_3$[F,Cl,OH]) has been studied for volatiles in K-, REE-, and P (KREEP), very high potassium (VHK), low-Ti and high-Ti basalts, as well as samples representing the lunar highlands [3-8]. These studies revealed a positive correlation between *in-situ* δ^{37}Cl measurements and bulk incompatible trace elements (ITEs) and ratios [7-8]. Such trends were interpreted to originate from Cl isotopic fractionation during the degassing of metal chlorides during or shortly after the differentiation of the Moon via a magma ocean. In this study, we investigate the mineralogical and textural occurrence of phosphates, and the volatile inventories of a group of samples for which new-era volatile data have yet to be reported – the high-titanium, high-potassium mare basalts (typically, >2000 ppm bulk K_2O).

Samples and Methods: We studied thin sections of three high-Ti, high-K basalts (also referred to as Type A basalts) from the Apollo 11 mission (10017, 10024, 10049). These samples have bulk K_2O contents between ~0.28 and 0.33 wt.%, P_2O_5 contents from 0.15 to 0.16 wt.%, and TiO_2 contents from 10.6 to 12.6 wt.% [11-12]. They represent a sampling of the end-members of the high-Ti, high-K basalt group, whilst also displaying variations in ITE abundances. The basalts have crystallization ages ranging from approximately 3.5 to 3.7 Ga [11 and references therein].

Thin sections were C coated and preliminary analyses and characterization work was conducted using the JEOL 7600F scanning electron microscope at JSC. Samples were initially X-ray mapped using energy dispersive spectroscopy (EDS) to locate P hotspots associated with the phosphates. Isotopic analyses of apatite in 10049 were conducted by isotope imaging on the JSC NanoSIMS 50L. The negative secondary ions of ^{18}O, ^{19}F, ^{31}P, ^{35}Cl, and ^{37}Cl were collected simultaneously with electron multipliers. A Cs+ primary beam of ~7 pA was rastered over a range of areas (~64 to 324 µm^2). Well characterized apatite standards with a range of OH, Cl, and F contents and of known Cl isotopic compostions were used as primary reference standards for calibrating both isotope ratios and volatile abundances.

Phosphates in high-K basalts: Apatite occurs as a late-stage mineral almost exclusively in mesostasis areas within the samples we investigated thus far. It typically coexists with plagioclase, high-Fe pyroxene, silica, ilmenite, troilite, K-rich residual glass, K-Ba feldspar, Zr-bearing minerals, and REE-merrillite. Apatite is present either as (i) discrete crystals varying from basal to acicular, most are euhedral with some being sub-hedral (Figure 1), and (ii) apatite-merrillite intergrowths. The intergrowths vary in texture from hexagonal crystals containing both phosphates typically within the mesostasis to vein-like merrillite with minor anhedral apatite, the latter are more commonly located at the boundary of, or cross-cutting through, the main rock-forming minerals (e.g. pyroxene). The observed intergrowth textures are strikingly similar to those reported in lunar highlands samples and KREEP-rich basalts [e.g., 13-14]. Apatite crystal size varies amongst the samples studied (which themselves vary from very fine to medium grained basalts) from <1µm to ~60 µm in the longest dimension.

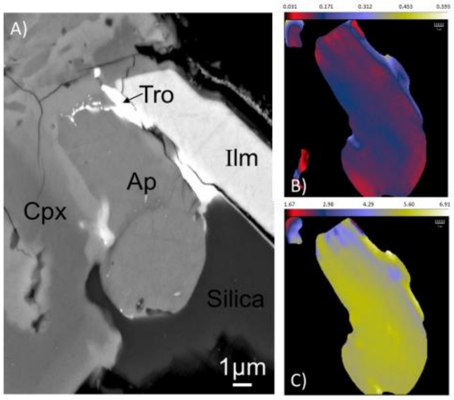

Figure 1: A) Backscattered electron image showing the petrographic setting of an apatite crystal in 10049. Tro = troilite, Cpx = clinopyroxene, Ap = apatite, and Ilm = ilmenite, B) Cl/P and C) F/P isotope ratio images. The color scale bars on the isotope images vary from low to high ratios from left to right (i.e., black to white).

Results of the isotopic analyses of high-K, high-Ti basalt: We used isotope imaging on the NanoSIMS to obtain the Cl isotopic composition [δ^{37}Cl (‰) = ((^{37}Cl/^{35}Cl$_{sample}$/^{37}Cl/^{35}Cl$_{standard}$) -1) × 1000)] of five apatite crystals in 10049, which ranges from ~ –2.7 ± 2 ‰ to +8.5 ± 1 ‰ (2σ). Using the volatile calibration determined by NanoSIMS analysis of apatite standards, the F content of the apatite crystals analyzed in 10049 varied from 3.16 to 3.7 wt.% and the Cl content from 0.02 to 0.21 wt.%.

Volatiles in high-Ti mare basalts: Of the high-Ti basalts (>9 wt.% bulk TiO_2) only members of the low-K sub-group have been investigated previously for $\delta^{37}Cl_{Ap}$: Apollo 11 samples 10044 and 10058, and Apollo 17 samples 70017, 70035, and 75055 [7-8,16] (Figure 2). In these samples apatite is most commonly fluorapatite, is usually located within late-stage mesostasis areas, and the samples are typically devoid of REE-merrillite. Of the mare basalts analyzed the high-Ti basalts show larger intra-sample H-isotope variations on the order of ~200 to 300 ‰ (2 SD) at relatively restricted OH contents when compared to low-Ti basalts [14-17]. In this volume, Barnes *et al.* [18] show that the same appears to be true for Cl-isotope compositions, with intra-sample variations on the order of 6 to 8 ‰ (2 SD), roughly double that observed for apatite in low-Ti mare basalts. Figure 2 shows the Cl-isotope compositions for apatite in lunar basalts compared with bulk rock Th abundances. In comparison to the high-Ti, low-K basalts, apatite from the most geochemically evolved [12] Apollo 11 high-K basalt (10049) show lighter $\delta^{37}Cl$ values, whilst displaying Th abundances similar to those of KREEP basalt 72275 (i.e., ~135 × C.I. chondrite).

Petrogenesis of the high-Ti basalts in light of Cl isotopes: Simply following the models of [7-8] for lunar rocks with high bulk abundances of ITEs we might expect the high-Ti, high-K basalts to contain apatite characterized by heavily fractionated Cl isotope compositions, i.e., Cl obtained from mixing between unfractionated mantle Cl (~ 0‰) and the urKREEP reservoir (possibly fractionated to >+25‰, [19]). However, the data obtained for 10049 do not conform to either the early degassing or mixing models (Figure 2). Current petrogentic models for the origin of the high-Ti, high-K basalts do not include urKREEP assimilation into the lunar magma ocean (LMO) cumulate sources. This is based on observations of (i) lower La/Sm ratios [12,20], (ii) relatively LREE-depleted profiles [12,20], and (iii) depleted initial Nd and Sr isotopic compositions [21] of the high-Ti, high-K basalts compared to KREEP. Neal and Taylor [20] suggested that source region heterogeneity rather than assimilation could explain the geochemical characteristics of the high-Ti mare basalts. In addition, the source regions for the high-Ti basalts may have been affected by metasomatism [22]. As Neal and Taylor [20] point out, if the hypothetical metasomatic agent was a KREEPy fluid, then that could explain the trend towards KREEP-like La vs K composition of Apollo 11 high-Ti, high-K basalts. Alternatively, assimilation of a lithology less evolved (lower La/Sm ratio) than KREEP could also reproduce the geochemical trends exhibited by the high-Ti, high-K basalts [e.g., 12]. The new data that we present provides evidence for the existence of regions in the lunar interior that are REE-enriched and contain Cl that does not share isotopic affinities with lunar urKREEP.

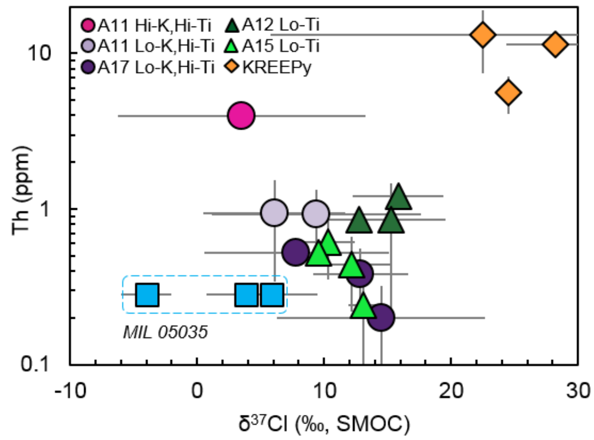

Figure 2: Average Cl-isotopic composition of apatite from Apollo lunar basalts [3-4,7-8,18] versus bulk rock Th abundances [11-12, additional references in 18]. The data points for low-Ti basaltic lunar meteorite MIL 05035 are the averages from multiple studies [4,7,18]. Uncertainties represent the standard deviation (2 SD) on reported values. SMOC refers to standard mean ocean chloride.

Acknowledgements: This work is supported by a NASA postdoctoral fellowship awarded to JJB and NASA's LASER program grant #NNX13AK32G awarded to F.M.M.

References: [1] Sharp Z. D. et al. (2007) *Nature 446*, 1062-1065. [2] Sharp Z. D. et al. (2013) *GCA 107*, 189–204. [3] Sharp Z. D. et al. (2010) *Science 329*, 1050–1053. [4] Wang Y. et al. (2012) *Proc. 75th Met. Soc.*, #5170. [5] Treiman A. H. et al. (2014) *Am. Mineral., 99*, 1860–1870. [6] Tartèse R. et al. (2014) *Meteoritics & Planet. Sci., 49*, 2266–2289. [7] Boyce J. W. et al. (2015) *Sci. Adv., 1*, e1500380. [8] Barnes J. J. et al. (2016) *EPSL* 447, 84-94. [9] Williams J. T. et al. (2016) *MaPS* 51, 2092-2110. [10] Sarafian A. et al. (2016) *EPSL* 459, 311-319. [11] Meyer, C. (2012). Lunar Sample Compendium, and references therein. [12] Hallis L. J. et al. (2014) *GCA* 134, 289-316. [13] Elardo S. et al. (2012) *GCA* 87, 154-177. [14] Tartèse R. et al. (2014) *Geology* 42, 363-366. [15] Greenwood J. et al. (2011) *Nat. Geosci.*, 4, 79-82. [16] Barnes J. J. et al. (2013) *Chem. Geol.*, 337-338, 48–55. [17] Tartèse R. et al. (2013) *GCA* 122, 58-74. [18] Barnes J. J. et al. (2017) Proc. XLVIII, this volume #1724. [19] Boyce J. W. et al. (2017) Proc. XLVIII, this volume #1618. [20] Neal C. R. and Taylor L.A. (1992) *GCA* 56, 2177-2211. [21] Gaffney A. M. et al. (2007) *GCA* 71, 3656-3671. [22] Paces J. B. et al. (1991) *GCA* 55, 2025-2043.